ALADYN: A method to investigate auroral arc electrodynamics from satellite data

O. Marghitu,[1,2] B. Klecker,[3] G. Haerendel,[4,2] and J. McFadden[5]

Received 12 March 2004; revised 29 July 2004; accepted 12 September 2004; published 10 November 2004.

[1] In the simplest representation of an auroral arc current system, the arc consists of a homogeneous block of increased conductance infinitely extended in longitudinal direction; field-aligned current (FAC) sheets that flow in and out of the ionosphere at the boundaries of the arc are connected through Pedersen current across the arc, while the electrojet (EJ) that flows along the arc as Hall current is divergence-free. To evaluate the deviation of the real arc current system from this ideal configuration, we developed the ALADYN (Auroral Arc Electrodynamics) method, based on a parametric model of the arc, that allows the derivation of the parameters by numerical fit to the experimental data. The method is illustrated with a wide, stable, winter evening arc, for which both Fast Auroral Snapshot (FAST) Explorer measurements at 3850 km altitude and ground optical data are available. We find that in order to obtain consistent results, one has to take into account, as a minimum, the ionospheric polarization, the contribution of the Hall current to the meridional closure of the FAC, and the coupling between the FAC and the EJ. *INDEX TERMS:* 2407 Ionosphere: Auroral ionosphere (2704); 2411 Ionosphere: Electric fields (2712); 2409 Ionosphere: Current systems (2708); 2455 Ionosphere: Particle precipitation; *KEYWORDS:* auroral arc, ionospheric electric field, arc current system, auroral electrojet, field-aligned current, particle precipitation

Citation: Marghitu, O., B. Klecker, G. Haerendel, and J. McFadden (2004), ALADYN: A method to investigate auroral arc electrodynamics from satellite data, *J. Geophys. Res.*, *109*, A11305, doi:10.1029/2004JA010474.

1. Introduction

[2] In order to get the electrodynamic description of the ionosphere in the vicinity of an auroral arc, one needs the Pedersen and Hall conductances, (Σ_P, Σ_H), the ionospheric electric field (IEF), **E**, and the height-integrated ionospheric current, $\mathbf{J}_\perp$. With satellite measurements, Σ_P and Σ_H can be computed from the particle data. If the satellite does not cross the Auroral Acceleration Region (AAR), **E** may be obtained, in principle, by mapping along the magnetic field line. Once the conductance and the IEF are known, $\mathbf{J}_\perp$ can be derived from Ohm's law. However, a medium-altitude satellite like FAST occasionally crosses the AAR. Then the magnetic field line below the satellite is no longer equipotential and the mapping does not work. In addition, the DC east-west electric field is not measured on FAST.

[3] The derivation of the IEF is particularly interesting at that times when the satellite is inside the AAR and ion beams are detected. By comparing the ion average energy with the field-aligned (FA) potential drop, one can investigate whether the electrostatic assumption for the FA potential holds [e.g., *McFadden et al.*, 1998; *Ergun et al.*, 2002]. In order to calculate the FA potential drop, one integrates the high-altitude electric field and the IEF along the satellite path and its ionospheric footprint, respectively, and then subtracts the high-altitude potential from the ionospheric one. The IEF is usually assumed to be constant across the ion beam. However, the north-south extension of the beam mapped at ionospheric level can be of several 10 km so that significant variations of the IEF due to polarization are in principle possible.

[4] The polarization of the arc in the presence of a westward electric field of magnetospheric origin was invoked by *de la Beaujardière et al.* [1977] to explain the often-observed relationship between the normal component of the IEF and the ionospheric plasma density in the vicinity of the arc: anticorrelation on the eveningside and correlation on the morningside. At about the same time, *Evans et al.* [1977] interpreted this feature in terms of FACs. The study of *de la Beaujardière et al.* [1977] was based on radar data, which allow the measurement of ionospheric ionization, while *Evans et al.* [1977] used rocket data, which give direct access to the precipitating particle flux.

[5] Later on, *Marklund* [1984] undertook a comprehensive review of the work published at that time and pointed out that polarization and FACs are just two complementary means of achieving the current conservation at ionospheric level, as already suggested by *de la Beaujardière et al.* [1981]. Depending on which of the two mechanisms prevails, *Marklund* [1984] identified polarization, Birkeland, and combination arcs, with each of the two mechanisms dominant at different arc locations for the third category.

[1]Institute for Space Sciences, Bucharest, Romania.
[2]Also at Max-Planck-Institut für extraterrestrische Physik, Garching, Germany.
[3]Max-Planck-Institut für extraterrestrische Physik, Garching, Germany.
[4]International University of Bremen, Bremen, Germany.
[5]Space Sciences Laboratory, University of California, Berkeley, California, USA.

0148-0227/04/2004JA010474$09.00

Marklund [1984] chose a "discrete" approach and treated the arc as a homogeneous basic unit, infinitely extended in longitudinal direction. Although this may help to emphasize the concepts, the interplay between polarization and FACs can be fully captured only with a "continuous" method.

[6] Such a method had been developed by *Coroniti and Kennel* [1972], but it addressed the auroral oval as a whole and used a theoretical model to calculate the precipitating particle flux. In contrast, *Marklund* [1984] concentrated on the smaller-scale arc features and relied on experimental data. More recently, a theoretical "continuous" exploration of the arc-associated electric field was given by *Karlsson* [2001]. In the (conceptually) "continuous" class one may also include the large variety of methods based on ground magnetometer and radar data [e.g., *Glassmeier*, 1987; *Untiedt and Baumjohann*, 1993, and references therein] or, more recently, on conjugated radar and multisatellite data [*Amm*, 2002]. While these methods provide two-dimensional (2-D) coverage, their spatial resolution is relatively poor ($\sim$10 km). Given the fact that the longitudinal extension of the arcs is 1–2 orders of magnitude larger than their width and the longitudinal inhomogeneity is accordingly small, 1-D high-resolution satellite data might offer a better "continuous" description of the arc than 2-D ground measurements, at least in the vicinity of the satellite ionospheric footprint.

[7] In order to ease the theoretical tractability, arc (as well as auroral oval) models often neglect the longitudinal inhomogeneity, and the physical quantities are assumed to vary only transverse to the arc. According to the traditional view on the 3-D current arc system, first suggested by *Boström* [1964] and later confirmed by rocket [e.g., *Sesiano and Cloutier*, 1976] and satellite [e.g., *Sugiura*, 1984] experiments, the FACs are continued in the ionosphere by Pedersen currents perpendicular to the arc while the electrojet flows, as divergence free Hall current, parallel to the arc. Besides neglecting the FAC-EJ coupling, which cannot be avoided for a finite arc, such models also disregard the Hall contribution to the meridional FAC closure, which is equivalent to neglecting the electric field parallel to the arc. The significance of this electric field component for a realistic arc model was discussed by, e.g., *Atkinson* [1982].

[8] The task we want to accomplish here is to build a "continuous" arc model, properly parameterizing the ionospheric polarization, the contribution of the Hall current to the meridional closure of the FAC, and the FAC-electrojet coupling, that is able to accommodate experimental data input. The parametrization we shall introduce makes possible the investigation of the arc and the assessment of the interplay between polarization and FACs down to length scales limited only by the resolution of the experimental data.

[9] In order to clarify the importance of the parameters, we shall explore several instances of the model, depending on reduced parameter sets. Data collected by FAST above a stable, wide, winter evening arc, will be used as test bed. Optical ground data available in conjunction with FAST enable an additional consistency check. The work is organized as follows: We start in section 2 by setting the theoretical basis; next, in sections 3 and 4, we present the experimental data and compute the ionospheric conductance induced by electron precipitation; section 5 is devoted to the evaluation of the arc models, while in section 6 we check in more detail several assumptions; we conclude, in section 7, with a summary and prospects for future development.

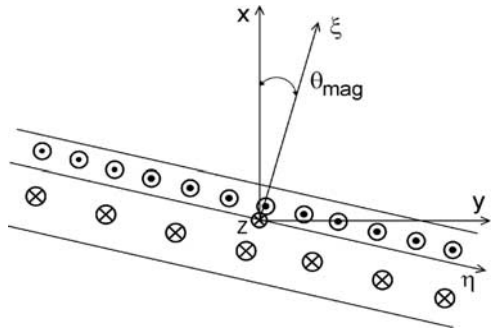

Figure 1. The (x, y, z) Satellite Associated System (SAS) and (ξ, η, z) Arc Associated System (AAS). The upward and downward current sheets are indicated with points and crosses, respectively. The ξ/η axes are shown perpendicular/parallel to the arc, but when θ is included among the fit parameters the AAS relates to the arc associated electrojet.

2. Theory

2.1. Current Closure in Cartesian Coordinates

[10] We shall use two reference systems, fixed in the inertial space: the (x, y, z) Satellite Associated System (SAS) and the (ξ, η, z) Arc Associated System (AAS). The two systems are shown in Figure 1 where, for simplicity, the downward and upward FAC sheets are parallel, with the downward sheet somewhat wider and less intense than the upward one. The z axis has the direction of **B** for both systems (we neglect the small inclination ($\sim$15°) of the auroral magnetic field lines with respect to the direction perpendicular to ionosphere). The x axis points along the ionospheric projection of the satellite velocity, while the ξ axis is perpendicular to the upward FAC sheet, as derived from satellite magnetic field data by minimum variance analysis. The y and η axes complete the respective right-handed systems and, for a polar satellite, both point roughly to the East. Note that when θ is included among the fit parameters ξ is not necessarily perpendicular to the arc. Strictly speaking, in this case the AAS relates to the arc associated electrojet (see section 2.4).

[11] By integrating the current continuity equation, $\nabla \cdot \mathbf{j} = \mathbf{0}$, between the top and the bottom of the ionosphere, one obtains

$$j_{\parallel}^{top} = \frac{\partial J_{\xi}}{\partial \xi} + \frac{\partial J_{\eta}}{\partial \eta}. \tag{1}$$

If Ampere's law is used to express $j_{\parallel}^{top}$,

$$j_{\parallel}^{top} = \left(\frac{\partial H_{\eta}}{\partial \xi} - \frac{\partial H_{\xi}}{\partial \eta} \right), \tag{2}$$

equation (1) becomes

$$\frac{\partial}{\partial \xi}\left(H_{\eta} - J_{\xi}\right) = \frac{\partial}{\partial \eta}\left(H_{\xi} + J_{\eta}\right). \tag{3}$$

By H, we mean $\Delta B^{ionos}/\mu_0$, with ΔB^{ionos} the measured magnetic perturbation mapped at ionospheric level. A similar form is obtained if the SAS is used instead of AAS. However, equation (3) is better suited to interpretation; $\partial H_\xi/\partial_\eta$ can be neglected if the satellite cross is not very far from the center of the current sheet (for an infinite current sheet $H_\xi = 0$ holds everywhere) and the right-hand side term reduces to $\partial J_\eta/\partial_\eta$. This is the variation of the electrojet current, and equation (3) says that the FAC closes not only transverse to the arc but also along the arc.

[12] In equation (3) the components of **J** can be expressed from the anisotropic Ohm's law

$$\mathbf{J} = \Sigma_P(\mathbf{E} + \mathbf{w} \times \mathbf{B}) - \Sigma_H(\mathbf{E} + \mathbf{w} \times \mathbf{B}) \times \mathbf{B}/B, \tag{4}$$

where $\mathbf{w} = \mathbf{w_{NW}} + \mathbf{w_{ER}}$ is the velocity of the neutral wind at E-layer altitudes, with respect to AAS and SAS, consisting of two contributions: the velocity with respect to the Earth, $\mathbf{w_{NW}}$ (which is currently measured by radars), and the velocity associated with the Earth's rotation, $\mathbf{w_{ER}}$. For the calculations to come we shall assume that $\mathbf{w} = \mathbf{0}$. This assumption will be discussed in more detail in section 6.1, where we will show that choosing $\mathbf{w} \neq \mathbf{0}$ does not lead to essential changes in the results.

[13] By introducing (4) in (3), one comes to a partial differential equation for E_ξ and E_η. *Sugiura* [1984] pointed out that a particular solution is obtained when the electric field is perpendicular to the current sheet and the Hall current along the arc is divergence free. One should not forget, however, that this is a special case, which is not necessarily verified by any data set. In order to get a more general solution, a proper parametrization of the IEF is required.

2.2. Parametrization of the IEF

[14] We shall assume the IEF to be electrostatic

$$\frac{\partial E_\eta}{\partial \xi} = \frac{\partial E_\xi}{\partial \eta} \tag{5}$$

and constant along η

$$\frac{\partial \mathbf{E}}{\partial \eta} = 0. \tag{6}$$

As an immediate consequence,

$$E_\eta = b_0 \equiv const, \tag{7}$$

which, if introduced in the rotation transform between AAS and SAS (**u** is an arbitrary vector),

$$\begin{aligned} u_\xi &= u_x \cos\theta + u_y \sin\theta \\ u_\eta &= -u_x \sin\theta + u_y \cos\theta \end{aligned} \tag{8}$$

leads to

$$E_y = E_x \tan\theta + b_0/\cos\theta. \tag{9}$$

In order to parametrize E_x, we write

$$E_x = E_{0_x} + \delta E_x = -\Delta\Phi/L + \delta E_x, \tag{10}$$

where E_{0_x} is the average IEF, while δE_x, not necessarily small, is associated mainly with the ionospheric polarization. Equation (10) assumes the magnetic field lines between the satellite and the ionosphere to be equipotential at the beginning and the end of the interval under study so that E_{0_x} can be calculated from the measured satellite data: $\Delta\Phi$ is the potential drop along the satellite path, while L is the length of the path ionospheric projection. The computation of $\Delta\Phi$ requires just the component of the electric field along the satellite velocity, which need not to be corrected for the satellite motion (adding $-\mathbf{v} \times \mathbf{B}$ only affects E_y, which we do not use as input data)

$$\Delta\Phi = -\int_{s_1}^{s_2} \mathbf{E} \cdot \mathbf{dx} = -\int_{s_1}^{s_2} \mathbf{E} \cdot \mathbf{v}\, dt, \tag{11}$$

with **v** the satellite velocity in the Geocentric Equatorial Inertial (GEI) system.

[15] A key issue is the parametrization of δE_x. We choose to write it as

$$\delta E_x = \sum_{i=1}^{n_x} a_i G_i, \tag{12}$$

where G_i are Legendre polynomials. The summation starts from 1 because the constant term, corresponding to index 0, was explicitly written as E_{0_x}. As the Legendre polynomials are defined for $-1 \leq x \leq 1$, the interval $[s_1, s_2]$ along the satellite path has to be mapped to $[-1, 1]$ by $x = 2(s - s_m)/(s_2 - s_1)$ with $s_m = (s_1 + s_2)/2$. The Legendre polynomials have the unique property that (see *Courant and Hilbert* [1953] for details)

$$\int_{-1}^{1} G_i = 0, \ \forall\, i \geq 1 \tag{13}$$

so that

$$\int_{s_1}^{s_2} \delta E_x\, ds = 0, \ \forall\, n_x. \tag{14}$$

By the form assumed for δE_x, one makes sure that independent of the expansion order n_x, the resulting E_x is consistent with the average IEF provided by the data, that is,

$$\int_{s_1}^{s_2} E_x\, dx = -\Delta\Phi. \tag{15}$$

In addition, because G_i are almost periodic except for the vicinity of the boundaries, if i is large enough ($i \gtrsim 10$), n_x can be associated with a polarization length scale

$$\lambda_{pol} \simeq \frac{L}{n_x}, \tag{16}$$

which is determined by the precipitation pattern. The proper choice of n_x will be further discussed in section 5.1.

2.3. Parametrization of the FAC-EJ Coupling

[16] As the data are only collected along the 1-D satellite path, solving the 2-D partial differential equation (3)

requires additional assumptions about the variation of the physical quantities along the arc. We have already set the constraint equation (6) on the IEF. A similar condition can be adopted for the current: the right-hand side term in equation (3) may be set equal to 0, which is equivalent to neglecting the FAC-EJ coupling. The simplest way to take the coupling into account is to assume this term to be constant

$$\frac{\partial}{\partial \eta}\left(H_\xi + J_\eta\right) = \widetilde{c_1} \Rightarrow \frac{\partial J_\eta}{\partial \eta} \simeq \widetilde{c_1}, \tag{17}$$

where $\widetilde{c_1}$ can be associated with the length scale of the electrojet

$$L_\eta \simeq \left|\frac{J_\eta}{\widetilde{c_1}}\right|. \tag{18}$$

Equation (3) can now be integrated

$$H_\eta - J_\xi = c(\eta) + \widetilde{c_1}\xi \simeq c_0 + \widetilde{c_1}\xi, \tag{19}$$

with the second form holding if the satellite displacement along the arc is small compared with the length scale of the electrojet. This is presumably the case for the satellites in polar orbits. The assumption $c(\eta) = c_0$ is further discussed in section 6.2.

[17] If the FAC-EJ coupling is neglected, a positive c_0 has the meaning of a background current that crosses the auroral oval, coming from the polar cap and leaving to the sub-auroral region. When the FAC-EJ coupling is included, $H_\eta - c_0$ is the transverse ionospheric current that feeds the arc system at the $\xi = 0$ boundary. In this case c_0 can no longer be associated with a constant background current because of the diversion into longitudinal direction.

2.4. Arc Models

[18] If equations (4), (8), (9), (10), and (12) are introduced in equation (19), the following fit equation results:

$$\begin{aligned} &H_x \tan\theta + \Sigma_P E_{0_x} \tan^2\theta + \Sigma_P\left(1+\tan^2\theta\right)\sum_{i=1}^{n_x} a_i G_i \\ &\quad + (-\Sigma_H + \Sigma_P \tan\theta) b_0 \sqrt{1+\tan^2\theta} + (c_0 + c_1 x)\sqrt{1+\tan^2\theta} \\ &= H_y - \Sigma_P E_{0_x}, \end{aligned} \tag{20}$$

with $c_1 = \widetilde{c_1}\cos\theta$. Equation (20) does not depend on y because the choice of the SAS reference system makes $y = 0$ along the satellite ionospheric footprint. The quantities on the right-hand side can all be derived from the measured data. An overview of the parameters on the left-hand side, to be derived by fit, is presented in Table 1. They are (1) the polarization coefficients a_i, (2) the Hall coefficient b_0, (3) the FAC-EJ coupling coefficient c_1, and (4) the current constant c_0. As already mentioned, the polarization order, n_x, can be tuned to the data (section 5.1). One can add $\tan\theta$ to the parameter list or compute it from the magnetic data by minimum variance analysis. In the first case the electrojet is free to flow along a direction which is not parallel to the arc (and, at the same time, the electric field is forced to stay constant along this direction). In the second case there is only one "privileged" arc direction, which may seem to be more intuitive. We shall return to a comparative discussion of the two situations in section 5.3.

Table 1. Fit Parameters

Parameter	Unit	Significance
a_i	mV/m	Polarization coefficients
b_0	mV/m	Tangential electric field
c_0	A/m	Current constant
c_1	μA/m^2	FAC-EJ coupling
$\tan\theta$[a]	adim.	Electrojet orientation

[a]Can also be computed from the magnetic field data.

Table 2. Hierarchy of Arc Models[a]

No FAC-EJ Coupling, $c_1 = 0$	FAC-EJ Coupling, $c_1 \neq 0$
NPNH(L)	NPNHX(L)
NPYH(L)	NPYHX(L)
YPNH(L)*n*	YPNHX(L)*n*
YPYH(L)*n*	YPYHX(L)*n*

[a]NP stands for "No Polarization" ($a_i = 0$), NH stands for "No Hall" ($b_0 = 0$), L stands for Linear ($\tan\theta$ from magnetic data), and X for the FAC-EJ coupling (which is expressed by the explicit dependence on x, the term $c_1 x$, in equation (20)).

[19] Equation (20) can be written in condensed form as

$$y_{ft_k} = y_{ms_k}, \tag{21}$$

where the indices "ft" and "ms" abbreviate "fit" and "measured", while "k" indicates that equation (21) is written for each measurement point. If $\tan\theta$ is considered as unknown, the fit equation is nonlinear in the parameters; these can be determined by the numerical minimization of a χ^2 type function

$$f = \sum_{k=1}^{N} \frac{\left(y_{ms_k} - y_{ft_k}\right)^2}{\sigma_k^2}, \tag{22}$$

where σ_k is the error in y_{ms_k} and N the number of measuring points; for $\sim$1 min of FAST Survey data $N \simeq 200$. If $\tan\theta$ is calculated from the magnetic data the fit equation becomes linear and the parameters can be also found by regression. The goodness-of-fit is measured by the reduced χ^2, defined as $\chi_r^2 = f/(N - M)$, with M the number of model parameters.

[20] Some of the parameters can be set to 0 in equation (20). Depending on this choice and also on how $\tan\theta$ is treated, one obtains a hierarchy of arc models, as presented in Table 2, where NP stands for "No Polarization" ($a_i = 0$), NH stands for "No Hall" ($b_0 = 0$), L stands for Linear ($\tan\theta$ from magnetic data), and X for the FAC-EJ coupling (which is expressed by the explicit dependence on x, the term $c_1 x$, in equation (20)). When the polarization is taken into account, n indicates the expansion order in equation (12).

[21] In order to provide a more intuitive representation of the fit quality, we introduce two new quantities, J_{ion} and J_{par}, as follows:

$$\begin{aligned} J_{ion} &= J_\xi + c_0 + \widetilde{c_1}\xi \\ J_{par} &= H_\eta. \end{aligned} \tag{23}$$

With these notations, equation (19) simply writes $J_{par} = J_{ion}$. As the fit equation (20) is equivalent to equation (19), by comparing J_{par} and J_{ion} (see section 5) one can get a "graphical measure" of the fit quality. If $\tan\theta$ is not included among the parameters, J_{ion} and J_{par} have a straightforward interpretation, assuming an ideal case with no FAC-EJ coupling and no background current ($\widetilde{c_1} = 0$, $c_0 = 0$); they represent the ionospheric current perpendicular to the arc, from the fit and measured magnetic data, respectively.

[22] Before proceeding further with a case study application of ALADYN, we feel the reader should be warned in advance that a good fit quality, i.e., a good agreement between J_{par} and J_{ion}, is not enough to validate a model. The formulation of this statement in statistical terms is that a small χ^2_r value just says that the model might be good but not that it is necessarily good. By including enough parameters, one can always end up with a small χ^2_r, even if, for example, relevant parameters are still missing. This point will be illustrated for a particular case in section 5, where additional consistency checks will be used to validate the models.

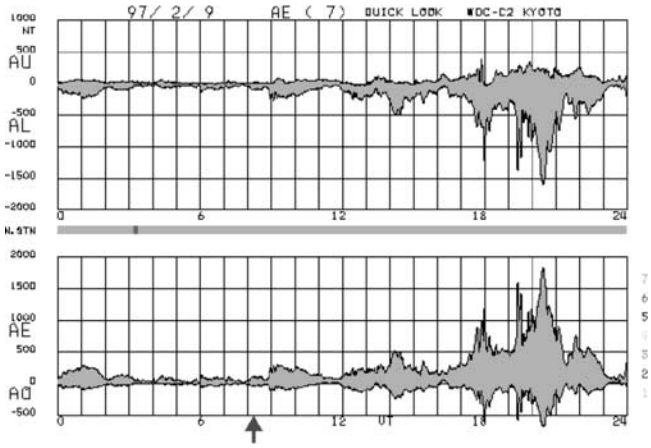

Figure 2. Auroral activity indices for 9 February 1997. From the World Data Center for Geomagnetism, Kyoto, http://swdcdb.kugi.kyoto-u.ac.jp. The arrow indicates the conjunction time.

3. Data

[23] During a winter campaign in January and February 1997, optical data in conjunction with FAST measurements were obtained for several FAST orbits. The ground equipment was located at Deadhorse, in northern Alaska (latitude 70.22°, longitude 211.61°). The data presented below were collected on 9 February 1997, around 0822 UT, at ~2100 MLT, above the evening auroral oval.

[24] FAST is the second Small Explorer NASA satellite [*Carlson et al.*, 1998] and was launched on 21 August 1996, in a 351 km × 4175 km polar orbit (83° inclination). The spacecraft executes a reversed cartwheel motion, with the spin axis perpendicular to the orbit plane, and it is equipped with a full set of instruments: high-resolution plasma analyzers (312 ms in survey mode and 78 ms in Burst mode, as well as uninterrupted 360° coverage in pitch-angle), a mass spectrometer, DC and AC magnetic and electric field detectors. A comprehensive description of the satellite and its payload can be found in a special issue of *Space Science Reviews* [*Pfaff et al.*, 2001, and references therein].

[25] The optical hardware was developed at Max-Planck-Institut für extraterrestrische Physik, Garching, and is based on low-light CCD cameras [*Frey et al.*, 1996]. The images used in this study were taken with the following setup: wide-angle optics, 86° × 64°, pass band filter, ≥650 nm, and exposure time 20 ms. The filter eliminates the long-lived emissions from atomic oxygen and allows for sharp images, a setup particularly useful for investigating highly dynamic structures. Although this is not our case, the setup is still convenient to get a reliable estimate of the arc velocity.

3.1. Geophysical Conditions

[26] The event under study occurred during an active period: a magnetic storm that started on 8 February was in progress and passed through its maximum ($D_{ST} = -68$) on 10 February at noon. The K_p index reached 6− on the afternoon of 8 February and 5+ on the evening of 9 February. However, the K_p for UT 0600–0900 was 2, the minimum value during this stormy period. The auroral oval was relatively quiet, as one can see in Figure 2 and as also witnessed by Polar UVI data. In agreement with Figure 2, ground magnetograms from Barrow and College show the enhancement of westward currents north of College, starting at ~0900 UT, which indicates that our data were collected during the growth phase of a small substorm.

3.2. FAST Data

[27] The satellite data above the auroral oval are dominated by the downward and upward FAC signatures. They are exhibited by Figure 3 and visible both in the magnetic field (Figure 3a) and in the particle data (Figures 3b–3e). The boundary between the large-scale downward and upward FACs is located at 0821:50, as indicated by the slope of the perturbation magnetic field, ΔB_y, turning from positive (downward current) to negative (upward current). The presence of upward narrow bursts of medium energy (1 keV) electrons is the most prominent feature of the downward current region. Across the upward current region, the electrons show a large inverted-V, encompassing several ion beams.

[28] The bottom panel of Figure 3 presents the high-altitude electric potential, obtained by integrating the measured electric field along the satellite track. Until 0822:04 the potential decreases, corresponding to sunward convection, and the ions show mirroring plasma sheet distribution. North of 0822:04, which can be identified as the time of the convection reversal, the dominant ion feature is the sequence of beams and conics of ionospheric origin. The dips in the potential associated with the ion beams do not map to ionosphere. The gap between 0822:37 and 0822:47 is due to bad quality electric field data, presumably caused by saturation in low-density plasma. The matching of the potential is described in section 5. A peculiar feature of the data is the close vicinity between the FAC and electric field reversal (cf. first and last panel); we shall return to this in section 5.4.

3.3. Optical Data

[29] The optical behavior of the arc during the minute 0822:00–0823:00 is presented in Figure 4, which shows a sequence of four frames, 20 s apart, each of them bearing

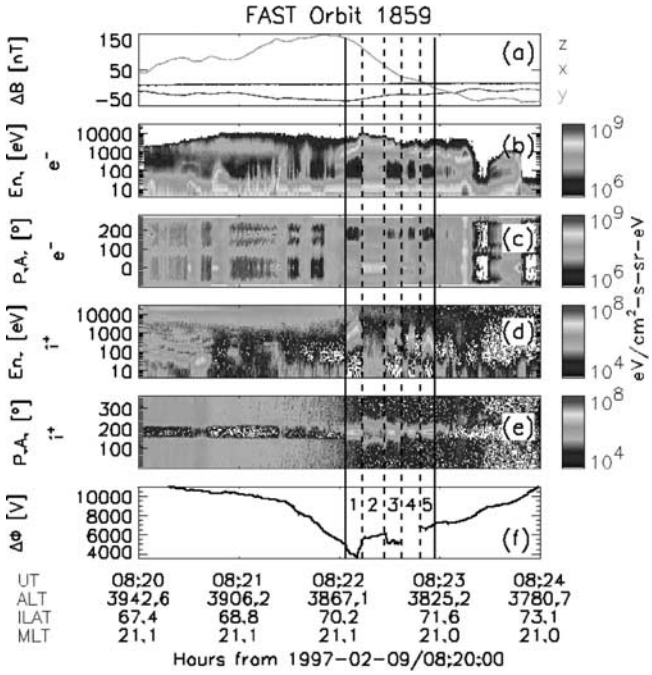

Figure 3. Medium-scale DC electromagnetic field and particles; the solid vertical lines indicate the ion beam interval, IALL, that will be used for the illustration of ALADYN; the dashed vertical lines show the subintervals I1–I5 (cf. Table 3). From top to bottom the figure shows (a) perturbation magnetic field, (b–e) electron/ion energy and pitch-angle spectrograms, and (f) potential drop along the satellite track. In Figures 3c and 3e the pitch-angle covers 360°, corresponding to the plasma instrument field of view; the angle range is shifted by 90° in Figure 3c to avoid having downward electrons split up among the plot borders. For the data gap in Figure 3f, see text. See color version of this figure at back of this issue.

markers for the satellite footprint and for the first two ion beams (placing beams' markers in all the frames does not imply that ion beams are necessarily there all the time and is just meant to provide a reference for the luminosity evolution). The ionospheric (110 km) footprint of the satellite was found by using the IGRF95 magnetic field model and further projected into the image plane. The association between viewing directions and image pixels was achieved by means of a procedure using well-known bright stars. The edge of the optical arc is seen to be coincident with the steep increase in the electron energy at 0822:10, which provides a cross-check for the mapping procedure.

[30] One notes the stability of the arc during the satellite overpass. In addition, by comparing the position of the southern edge of the arc with the position of the first ion beam, one can see that the arc has a slow, approximately uniform equatorward motion. The arc covers a distance roughly equal to half of the beam width in 1 min, which results in an average north-south velocity of ~200 m/s. A slow equatorward motion is known since long ago to be related to the growth phase of a substorm [e.g., *Mozer*, 1971]. If the arc is frozen in the ionospheric plasma (possible deviations from this assumption are discussed in section 5.3), the electric field associated with this motion points westward, has a magnitude of ~10 mV/m, and drives a northward Hall current. The east-west ionospheric plasma motion, associated with the north-south electric field, cannot be inferred from the optical data.

4. Ionospheric Conductance

[31] An essential ingredient in deriving the full picture of the ionospheric electrodynamics, for either large-scale, medium-scale, or small-scale phenomena, is the conductivity, which can be height-integrated to obtain the conductance. Satellite measurements, like those presented above, allow the monitoring of the particle influx into the ionosphere and the subsequent determination of the conductance. In the winter nighttime auroral region the conductance is essentially induced by particle precipitation.

4.1. Particle-Induced Conductance

[32] By fitting experimental results, *Robinson et al.* [1987] and *Galand et al.* [2001] found approximate formulas for Σ_P, Σ_H, induced by electrons and protons respectively. During our inverted-V event, proton contribution is negligible and the conductance induced by electron writes

$$\Sigma_P = \frac{40\overline{W}}{16+\overline{W}^2}\Phi_W^{1/2}, \qquad \frac{\Sigma_H}{\Sigma_P} = 0.45\overline{W}^{0.85}, \tag{24}$$

where Φ_W is the energy flux in erg/cm^2·s and $\overline{W}$ is the average energy in keV, calculated as ratio of energy to number flux

$$\overline{W} = \frac{\Phi_W}{\Phi_N} = \frac{\int_{W_{\min}}^{W_{\max}} WF(W)\,dW}{\int_{W_{\min}}^{W_{\max}} F(W)\,dW}. \tag{25}$$

In the equation above, $F(W)$ is the differential number flux and $W_{\min}$, $W_{\max}$ are the lower and upper integration limits,

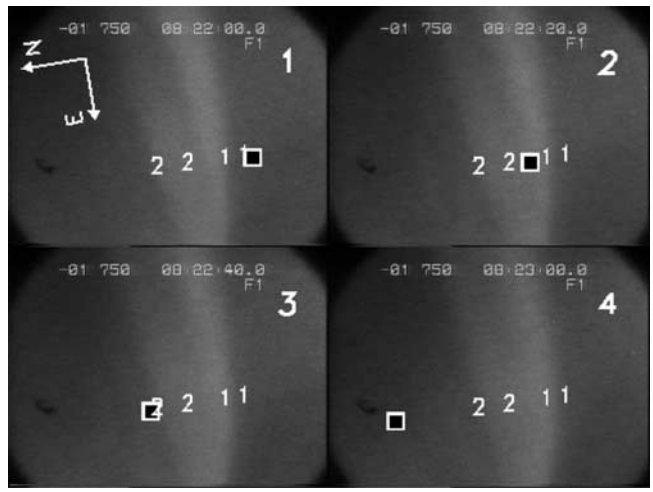

Figure 4. Optical images 20 s apart taken during the FAST overpass. The satellite is shown as a square and the limits of the first two ion beams are indicated in each image as "11" and "22." Note the equatorward drift of the southern edge of the arc.

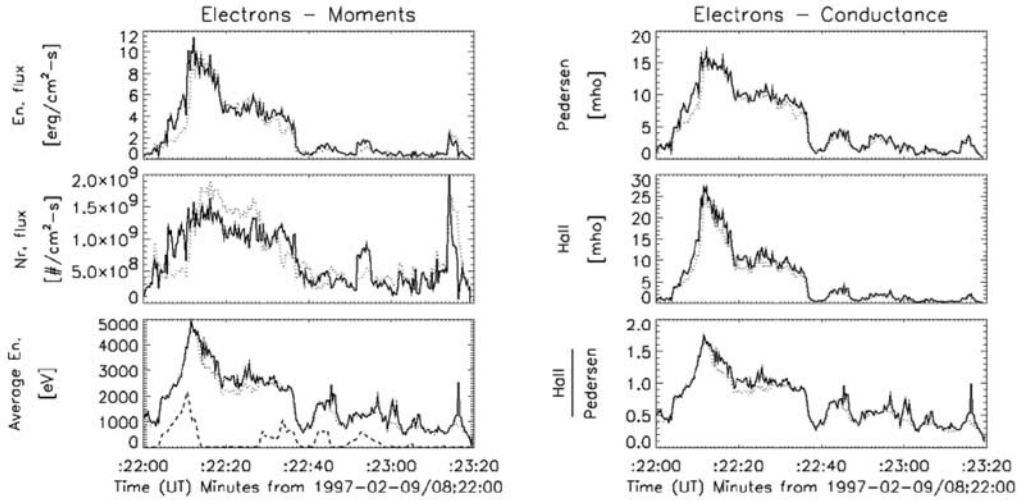

Figure 5. (left) Electron energy flux, number flux, and average energy, at ionospheric level, under the inverted-V. (right) Σ_P, Σ_H, and the ratio Σ_P/Σ_H, calculated from equation (24), by using Φ_W and $\overline{W}$ from the left plot. Black solid lines (red dots) indicate integration over the full velocity space (loss cone). In the bottom left panel the ion beam average energy is shown with black dashes. See color version of this figure at back of this issue.

which depend on the detector characteristics. Following *Robinson et al.* [1987], we chose $W_{\min} = 500$ eV and $W_{\max} = 30$ keV (the upper limit of the detector), a range that fully covers the inverted-V electrons (whose energy is ≤ 5 keV).

[33] The conductance estimates given by equation (24) were obtained by processing radar data, essentially ionospheric ionization. This is produced by the energetic electrons "captured" in the ionosphere, i.e., the incident flux, available at the top of the ionosphere, minus the reflected flux (backscattered and secondaries). In order to get the flux that actually dissipates in the ionosphere, from FAST data measured at 4000 km altitude, one has to integrate over the full distribution. The conductance obtained this way will be used in section 5 for the models' evaluation. In addition, we also computed the conductance by integration over the loss cone. This will serve in section 6.3 to check the sensitivity of our results to the accuracy in the conductance. In integrating over the loss cone, we did not take into account its widening produced by the potential drop below the satellite (when ion beams are detected). As discussed in the last paragraph of this section, this lack of rigor turns out to be convenient.

[34] In the left plot of Figure 5 we show Φ_W, Φ_N, and $\overline{W}$. All the quantities were mapped to ionosphere

$$\Phi_W^{ionos} = \frac{B^{ionos}}{B^{sat}}\left(\Phi_W^{sat} + \Phi_N^{sat} e U^{below}\right)$$
$$\overline{W}^{ionos} = \overline{W}^{sat} + eU^{below}. \tag{26}$$

We took eU^{below} equal to the average ion energy during ion beams and 0 for the rest of the time. When $U^{below} = 0$, equation (26) reduces to the mapping required by the convergent magnetic field.

[35] The fluxes obtained by integration over the full distribution are lower outside of the ion beams because of the negative source cone contribution that adds to the fluxes yielded by integration over the loss cone. Inside the ion beams the relation is reversed: the widening of the loss cone enhances the fluxes, overcompensating the negative contribution of the (also widened) source cone. The average energy is sensitive to the integration domain only outside of the beams, where backscattered and secondary electrons make a significant difference to the number flux but not to the energy flux.

[36] The Pedersen and Hall conductances, as well as their ratio, are shown in the right plot of Figure 5. We note that the fluxes, and consequently the conductance, obtained for the two integration domains would exhibit little difference inside the ion beams, if we used the widened loss cone. In order to check the dependence of the results on the conductance, the profile that we obtained by neglecting the widening of the loss cone is, however, more appropriate. This is in particular valid inside the first ion beam, where the integration over the (not widened) loss cone yields a lower conductance, which may be closer to the actual value there; at the leading edge of the arc the actual conductance is presumably smaller than the one yielded by equation (24), based on the stationarity assumption.

4.2. Errors in Conductance

[37] For a good electrodynamic description of the auroral arc, one needs to evaluate the accuracy of the conductance calculation, which is affected by methodological and measurement errors. The methodological errors result from the chain of approximations implied by equation (24), while the measurement errors are related mainly to the statistical nature of the particle experiment.

[38] The reader is referred to *Marghitu* [2003] for an extended discussion of the errors affecting the calculation of the conductance. It is shown there that by applying the error propagation formula to the actual, measured distribution, one can expect to get a reasonable estimate of the error variation along the satellite path. The measurement errors are quite small under the energetic part of the inverted-V,

Table 3. E_{0_x} During the Ion Beam Period of Orbit 1859

Id	Δt	L, km	$\Delta\Phi$, V	E_{0_x}, mV/m
I1	03.8–13.8	28.5	482	−16.9
I2	13.8–26.9	36.7	455	−12.4
I3	26.9–37.7	30.5	(500, 350)	(−16.4, −11.5)
I4	37.7–48.5	30.5	(500, 350)	(−16.4, −11.5)
I5	48.5–57.5	26.1	292	−11.2
IALL	03.8–57.5	152.3	(2229, 1929)	(−14.6, −12.7)

inside the visible arc, and increase at the edges. This behavior is similar to the expected variation of the methodological errors: assuming stationarity at the edges of the arc (implicit in equation (24)) is presumably more error prone than inside the arc. The measurement error can be used as proxy for the variation profile of the error across the arc. As we will discuss in section 6.3, the precise knowledge of the error is expected to have little influence on the results, except for the intervals of low conductance.

5. Evaluation of the Models

[39] Once the conductance is available, one can proceed to the calculation of the IEF by fitting the hierarchy of models associated with equation (20) to the experimental data. We shall illustrate ALADYN by deriving the ionospheric electric field and current for the ion beam period of FAST orbit 1859, IALL = 0822:03.8–0822:57.5. In order to estimate E_{0_x} over IALL, given the gap in the electric field data, we used the fact that IALL consists of an alternation of ion beams (IB) and ion conics (IC) and can be naturally divided in five roughly equal subintervals. The second column of Table 3 shows the respective time periods. The time origin is $t_0 \equiv$ 0822:00. Note that I4 consists of two conics and one beam, whereas the other intervals cover either beams (I1, I3, I5) or a conic (I2). Column 3 of the table shows the length of the satellite path projected to ionosphere. Columns 4 and 5 show the potential difference across each path segment and the corresponding E_{0_x}. For I3 and I4 some reasonable upper and lower limits are indicated, based on the values for the other three intervals.

[40] The results in sections 5.1 and 5.2 below correspond to the models which assume θ as parameter, thus giving the minimization procedure more freedom in finding the "minimum energy" point of the data configuration. As we shall see, this leads to a relatively large angle between the electrojet and the arc. By using θ as inferred from the magnetic data, one implicitly requires that the electrojet flows parallel to the arc. The electric field and current obtained this way are discussed in sections 5.3 and 5.4.

5.1. Models NPNH, NPYH, and YPNH

[41] If the polarization or the Hall contribution or both are neglected, one cannot expect to obtain consistent results. The highly structured auroral precipitation induces steep gradients in the conductance, which lead to ionospheric polarization. The Hall contribution, in its turn, is known to be a key ingredient in the development of a partial Cowling channel, which is often colocated with the arc. Still, considering these "incomplete" models provides a good reference that helps in judging the more involved instances.

[42] Figure 6 shows the results obtained for the models NPNH and NPYH: J_{par} versus J_{ion} (equation (23)) in the top line and the components of the IEF in the bottom line. For model YPNH we examined in addition the influence of the polarization length scale, which depends on the expansion order, n_x (equation (16)). Numerically, one can get to quite large n_x values, but in practice a reasonable "threshold" can be determined from the data, by fitting y_{ms} with progressively higher-order expansions. The dependence of χ_r^2 on n_x is shown in the top left panel of Figure 7. The decrease of χ_r^2 is seen to saturate at $n_x \approx 18$; for higher orders the

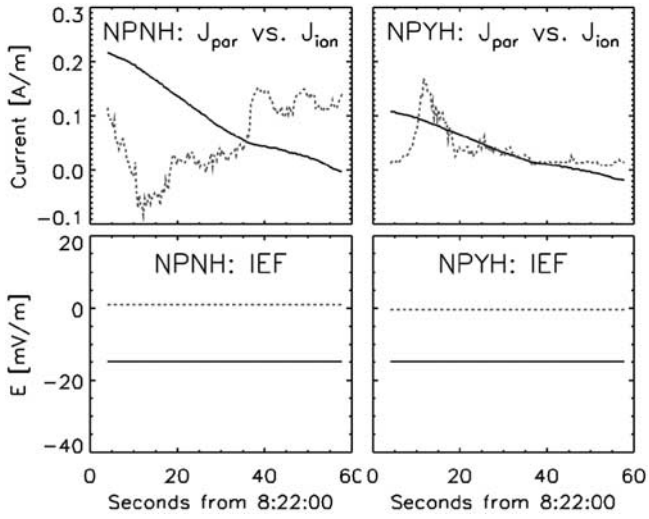

Figure 6. Fit results obtained for models NPNH (left) and NPYH (right). In the top line we compare J_{par} and J_{ion} (equation (23)); the bottom line shows the components of the IEF, E_x and E_y. J_{par} and E_x are plotted solid, while J_{ion} and E_y are dashed.

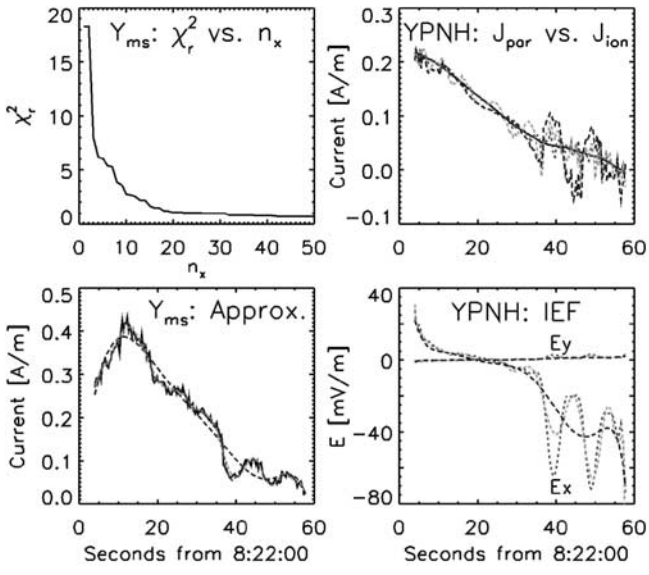

Figure 7. (top left) Dependence of χ_r^2 on the expansion order for y_{ms}. (bottom left) Approximations of the measured data, y_{ms} (black solid), with orthogonal polynomials. (right) Fit results obtained for model YPNH; J_{par} is plotted black solid. In the bottom left and in the right panels blue long-dashes/green dash-dots/red dashes stand for n_x = 7/18/36. See color version of this figure at back of this issue.

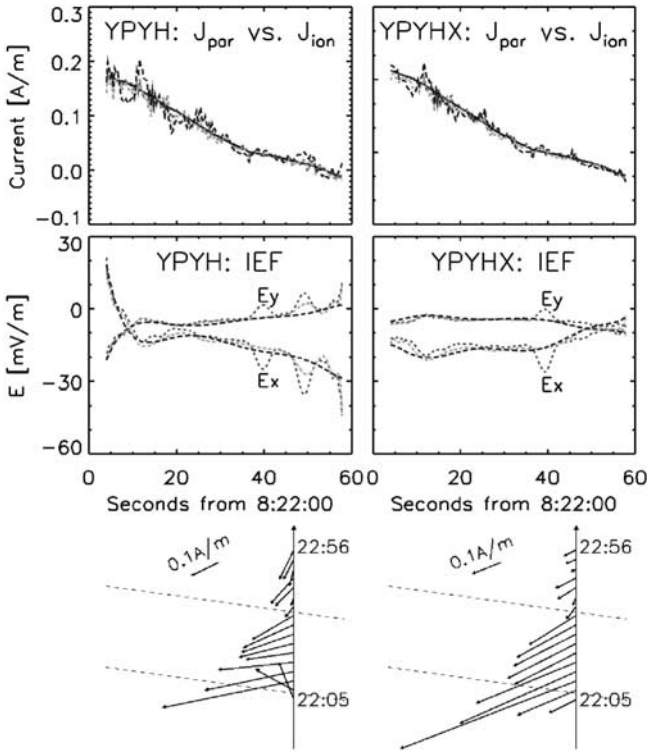

Figure 8. Fit results obtained for models YPYH (left) and YPYHX (right). (top) Fit quality, J_{par} versus J_{ion}; (middle) Electric field for n_x = 7/18/36; (bottom) Ionospheric current along the satellite footprint for n_x = 36. The color-line style convention in the top and middle panels is the same as in Figure 7. See color version of this figure at back of this issue.

relative improvement is small but, as we shall see below, the higher orders are needed in order to capture the fine structures. The bottom left panel of Figure 7 shows y_{ms} together with the approximations obtained for n_x = 7, 18, 36. The small-scale variability in y_{ms} results from the electron precipitation: the decrease of χ^2_r saturates at $n_x \approx 4$ for H_y and at $n_x \approx 18$ for Σ_P. The fit quality (measured by the difference between J_{par} and J_{ion}) and the IEF components obtained for the model YPNH are presented in the right panels of Figure 7.

[43] From Figures 6 and 7 it is evident that the fit gets better with the sophistication of the model. A significant improvement is achieved already for model NPYH, which gives a good hint on the importance of the Hall term. When the polarization is taken into account the agreement between fit and experiment is almost perfect at high polarization orders, but E_x exhibits a decreasing trend which is not supported by the high-altitude data. In addition, $E_y \simeq 0$, which implies negligible plasma convection in north-south direction. As the arc drifts southward at a speed of ~200 m/s (section 3.3), this means that the motion of the arc with respect to the plasma, the arc proper motion, is relatively fast.

5.2. Models YPYH and YPYHX

[44] The results get improved when both the polarization and the Hall contribution to the meridional closure of the FAC are taken into account. In Figure 8 we show the fit quality (top) and the electric field (middle), depending on the polarization order, as well as the ionospheric current along the satellite footprint for n_x = 36 (bottom). The electric field does not depend significantly on n_x, except for the short intervals of low conductivity at the trailing edge of the arc, which are properly modeled only for n_x = 36. Note that the polarization length scale corresponding to n_x = 36 is ~4 km. This distance can be resolved by our Survey FAST data, which have a spatial resolution at ionospheric level of ~900 m.

[45] Judging from Figure 8, one cannot make an unequivocal choice between the models YPYH and YPYHX: the fit quality is good for both of them and the electric field has reasonable values. Near the leading edge of the arc, at 0822:10, E_y is in both cases equal to ~5 mV/m westward, which implies a reasonable proper motion at a speed of ~100 m/s. Although the visual inspection would recommend model YPYHX because the electric field looks more consistent with the high-altitude data and the current vector is well-behaved at the edges of the arc, more thorough consistency checks are required in order to test the validity of the two models.

[46] A good IEF should integrate to a potential that matches the high-altitude potential outside of the ion beams. In addition, E_x and E_y should not depend on the choice of the fit interval. The integration smoothes out the small disagreements and, by comparing the potentials, one gets an overall figure of merit. The examination of the results with respect to the fit interval provides a better view on the details.

[47] The high-altitude and ionospheric potentials for model YPYH36 are shown in the left panel of Figure 9. The ionospheric potential covers the interval IALL while the high-altitude potential includes some 15 s before and after IALL. The jump in the high-altitude potential over the time interval with bad data is such that the potential drop over IALL is 2250 V. It is obvious that the model fails to reproduce the data, in particular over the intervals I1 and I5. The results are considerably improved for model YPYHX36, as seen in the right panel of Figure 9. The ionospheric and high-altitude potentials match each other and the drops across the ion beam intervals are roughly the same at the two levels.

[48] The comparison between the high-altitude potential, derived from measured FAST electric field, and the ionospheric potential, derived from fitted IEF, provides an important piece of evidence in favor of the model YPYHX.

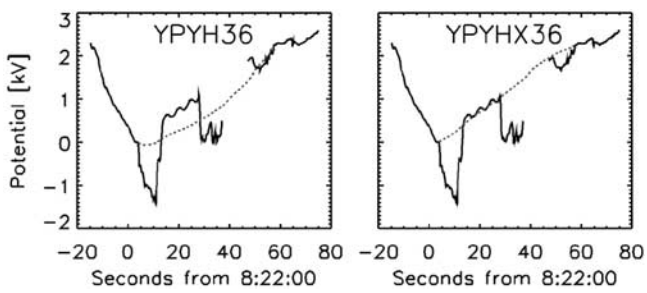

Figure 9. Internal consistency check for the models YPYH (left) and YPYHX (right). High-altitude potential (solid) versus ionospheric potential (dashes).

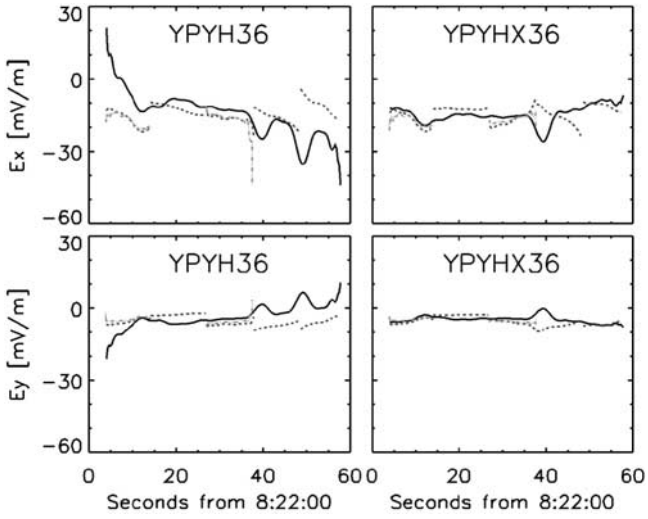

Figure 10. Internal consistency check for the models YPYH (left) and YPYHX (right): E_x (top) and E_y (bottom) obtained from fit over IALL (black solid) and over the subintervals I1–I5 (red dashes). The fit over I1 and I3 was also performed with Burst data, available during these intervals (green dash-dots). See color version of this figure at back of this issue.

We emphasize that just the total potential drop over IALL was supplied as input to the fit procedure. The detailed distribution of the ionospheric potential over the subintervals I1–I5 is related to the arc model.

[49] The dependence of the electric field on the fit interval was examined by comparing the IEF obtained over IALL, for $n_x = 36$, with that obtained over I1–I5, for $n_x = 7$ (Figure 10). As IALL is ~5 times longer than the subintervals, the choice of n_x makes the fit resolutions comparable. There is no free parameter to allow the matching of the separate curves. The fitted IEF obtained by using Burst data and $n_x = 28$ was added for I1 and I3, when the high data rate was on. As expected from the potential calculation, model YPYH yields a substantial disagreement for I1 and I5. The results get better for model YPYHX, except for the time around $t_0 + 39$. This is probably a numerical effect because the boundary between I3 and I4 lies in a low conductance region. With larger subintervals that include this boundary, most of the disagreement disappears. When Burst data are available, the results are similar to those obtained with Survey data except, sometimes, for the boundaries of the fit interval. We shall discuss the possible origin of the boundary effects in section 6.4.

5.3. Model YPYHXL: IEF

[50] By fitting the data to model YPYHX36, one obtains $\tan\theta = -0.4$, which implies $|\theta| \simeq 22°$ (see the bottom right panel of Figure 8). Although the experimental evidence suggests that sometimes the electrojet can flow at an angle with respect to the arc [e.g., *Evans et al.*, 1977], the other situation, when the electrojet and the arc are parallel, seems to be more common and more intuitive. In this case, $\tan\theta$ is no longer a fit parameter but derived from the magnetic data and, as already mentioned, the parameter set (a_i, b_0, c_0, c_1) can be found by linear regression. A cross-check that yielded identical results was performed by the nonlinear minimization of the (now quadratic) function f in equation (22).

[51] In order to derive $\tan\theta$ from the magnetic field data, we used the minimum variance analysis [e.g., *Sonnerup and Scheible*, 1998, and references therein]. Applying this method to the full interval IALL yields $\tan\theta = 0.14$, $\theta \simeq 8°$. Alternatively, it is possible to get a "continuous" variation of $\tan\theta$ by applying the minimum variance analysis over a time window sliding along IALL. If the width of the window is chosen to be 10 s, roughly equal to the time scale associated with the ion beam sequence, one gets $-0.15 \lesssim \tan\theta \lesssim 0.2$. As seen in Figure 11, the IEF is not very sensitive to the exact value of $\tan\theta$.

[52] In Figure 11 we also compare the IEF yielded by the models YPYHXL36 and YPYHX36. E_x and the ionospheric potential do not depend too much on the model. It is noteworthy that both models indicate variations in E_x at the edges of the visible arc, with the more substantial one at the trailing edge, where the gradient in conductivity is steeper. One also notes that E_x has a unipolar structure at the arc edges, which indicates adjacent layers of negative and positive polarization charges. An outline of the arc, including the charge layers at the edges, is shown in the bottom right panel of Figure 11. The polarization electric field is concentrated inside the double layers at the arc edges and makes little contribution to the electric field across the arc. This configuration is different from that of a Cowling

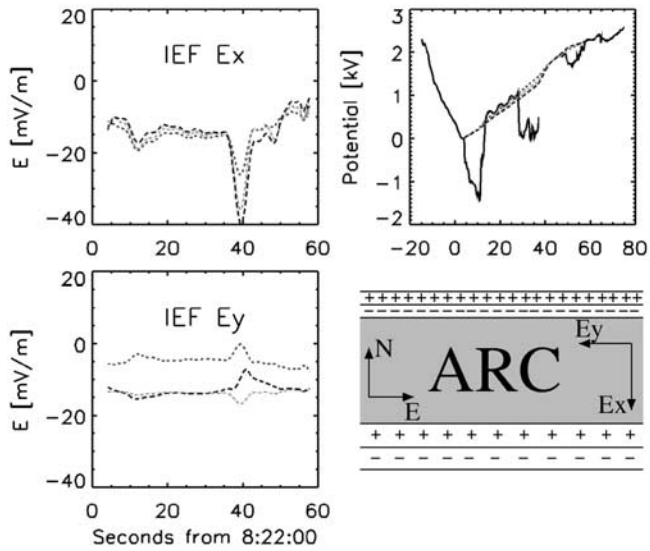

Figure 11. Comparison between the ionospheric electric field and potential obtained with models YPYHX36 (red dashes) and YPYHXL36, by applying minimum variance analysis over IALL (green dash-dots) and over a sliding 10 s window (blue long dashes). In the top right panel the high-altitude potential (black solid) is plotted for reference. The bottom right panel shows an outline of the arc, including the polarization charge double layers associated with the divergence of the electric field at the arc edges. At the southern edge of the arc the double layer is wider and less intense than at the northern edge, as indicated by the E_x panel. See color version of this figure at back of this issue.

channel, where the unipolar charge layers at the arc edges produce an electric field across the arc. In our case, the IEF inside the arc, between 0822:18 and 0822:36, is pretty flat and has about the same magnitude as outside of the arc. The polarization electric field is negligible and the closure of the current is achieved by FAC. According to the classification in the work of *Marklund* [1984], our arc (strictly speaking, the inside of the arc) would best fit in the IIc, noncorrelation category. The arc exhibits, however, an important peculiarity: while in the work of *Marklund* [1984] the current closure is achieved transverse to the arc, in our case the current closes along the arc, at least in the vicinity of FAST ionospheric footprint, as discussed in section 5.4.

[53] E_y depends on the model and its change can be explained (section 5.4) with the change in the orientation of the ionospheric current. In both cases there is a slight disagreement, δE_y 5 mV/m, compared with the value inferred from the optical data, which suggests proper motion of the arc: the plasma drifts somewhat faster than the arc for model YPYHXL36, and somewhat slower for model YPYHX36. *Haerendel et al.* [1993] pointed out that the proper motion of the arc can be related to the magnetic energy content in the magnetosphere-ionosphere current circuit. They assumed that downward and upward FACs are connected to a generator region in the magnetosphere and closed (dominantly) by Pedersen current in the ionosphere. The current circuit can expand/shrink because of plasma inflow/outflow at generator and/or AAR level. Magnetic energy builds up (as appropriate during the growth phase of a substorm) when the circuit expands and is released (as appropriate during the expansion phase) when the circuit shrinks. This argument seems to favor model YPYHXL36 (plasma flow into the current circuit during the growth phase), but the reader is cautioned that it is not directly applicable here; as discussed below, the downward and upward FACs are decoupled in the vicinity of FAST ionospheric footprint, instead of being connected through Pedersen current transverse to the arc, as required by *Haerendel et al.* [1993]. In addition, the arc proper motion depends, to some extent, on the velocity assumed for the neutral wind (section 6.1).

5.4. Model YPYHXL: Current Configuration

[54] The ionospheric current vector along the FAST footprint for model YPYHXL36 (tan θ from minimum variance analysis with 10 s window) is shown in the left plot of Figure 12 and, as expected, is on average parallel to the arc. The change in the orientation of the ionospheric current explains why E_y is increased compared to model YPYHX36. The sketch in the right plot of Figure 12, where $(\mathbf{E_1}, \mathbf{J_1})$ are associated with model YPYHX and $(\mathbf{E_2}, \mathbf{J_2})$ with model YPYHXL, serves helping the explanation. The average conductance ratio over IALL is $\langle \Sigma_H/\Sigma_P \rangle \simeq 1$, which implies that $\langle \theta_1 \rangle \simeq \langle \theta_2 \rangle \simeq 45°$. In addition, $\mathbf{E_1}$ and $\mathbf{E_2}$ are related by $\langle E_{1_x} \rangle = \langle E_{2_x} \rangle = E_{0_x}$. With $\tan \theta_{J_1} = 0.5$, $\tan \theta_{J_2} = 0$, and $|E_{0_x}| \simeq 15$ mV/m, one obtains $|E_{1_y}| \simeq E_{0_x}/\tan(\theta_{J_1} + \theta_1) \simeq$ 5mV/m and $|E_{2_y}| \simeq E_{0_x}/\tan\theta_2 \simeq 15$ mV/m, in good agreement with the fit results.

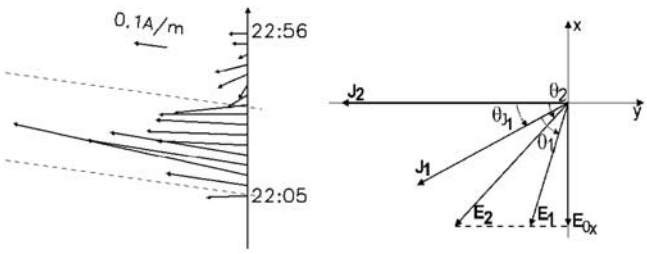

Figure 12. (left) The current along the ionospheric footprint of FAST for model YPYHXL36. (right) Sketch that serves to explain why E_y is larger for model YPYHXL36, compared with model YPYHX36.

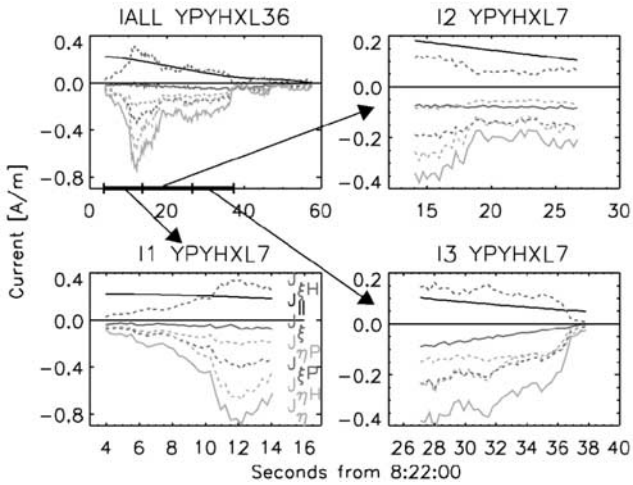

Figure 13. The FA and ionospheric sheet currents, along the FAST footprint, resulting from model YPYHXL. The Pedersen and Hall components of J_ξ (red) and J_η (green) are shown with dashed lines and are labeled in the bottom left panel. (top left) Fit over IALL. (bottom and top right) Fit over the intervals I1, I2, and I3 that encompass the visible arc. J_ξ during I1 is very small, indicating a negligible ionospheric current transfer between the downward and upward FACs. See color version of this figure at back of this issue.

[55] A different view over the ionospheric current is offered by Figure 13, where the components perpendicular and parallel to the arc, J_ξ and J_η, are presented together with their respective Pedersen and Hall contributions, $(J_{\xi P}, J_{\xi H})$ and $(J_{\eta P}, J_{\eta H})$. We show the currents for IALL and the subintervals I1, I2, I3 that encompass the visible arc. A peculiar feature is that J_ξ stays very small during I1, where $J_{\xi P}$ and $J_{\xi H}$ compensate each other, which indicates that the downward and upward FAC sheets are decoupled near the FAST ionospheric footprint.

[56] The topology of the current flow looks quite surprising, the more so as the magnetic field signature suggests a standard evening configuration, with downward FAC south of the arc, connected by ionospheric Pedersen current to the upward FAC above the arc. The standard view on the auroral arc current system, originating with *Boström* [1964] and validated since then by a large variety of in situ [e.g., *Sugiura*, 1984], ground [e.g., *Opgenoorth et al.*, 1990; *Aikio et al.*, 1993], and conjugated measurements [e.g., *Janhunen et al.*, 2000], does not hold in our case, at least in the vicinity of FAST footprint. Strong evidence supporting this conclusion is provided by an outstanding feature exhibited by the

data (Figure 3), namely the close proximity of the convection and FAC reversal. It is only in the narrow strip between these two boundaries that a minor part of the current injected into ionosphere by the downward FAC joins the upward FAC. The subsequent atypical current configuration will be examined in detail in an upcoming publication.

6. Additional Comments

6.1. Influence of the Neutral Wind

[57] The results in section 5 were obtained by setting $\mathbf{w} = 0$ in equation (4), that is, we assumed the neutral wind velocity with respect to the Earth, $\mathbf{w_{NW}}$, is equal and opposite to the rotation velocity of the Earth, $\mathbf{w_{ER}}$. In order to check the influence of the neutral wind, we repeated the calculations for the case when the neutral atmosphere rotates with the Earth, $\mathbf{w_{NW}} = 0$, $\mathbf{w} = \mathbf{w_{ER}}$. At auroral latitudes ($\sim 70°$) $\mathbf{w_{ER}} \simeq 160$ m/s, which is equivalent to a northward electric field $E \simeq 8$ mV/m. This implies a change of the average electric field over IALL from $E_{0_x} \simeq -15$ mV/m to $E_{0_x} \simeq -7$ mV/m. The main consequence of this change is a reduction of the magnitude of E_x with ~ 8 mV/m without, however, significant changes in the variation pattern. This is not surprising, given the fact that this pattern is controlled by the conductance and in the fit input term, $H_y - \Sigma_P E_{0_x}$ (right-hand side of equation (20)), E_{0_x} is just a scale factor for the conductance. Although E_x changes, our main conclusion does not change: consistent results are obtained only when the polarization, the electric field parallel to the arc, and the FAC-EJ coupling are taken into account.

[58] In addition to the change in E_x, there are also small changes in the other parameters, which together lead to a decrease in the magnitude of E_y (equation (9)): model YPYHX yields a westward IEF component of ~ 2 mV/m instead of ~ 5 mV/m, while model YPYHXL yields ~ 7 mV/m instead of ~ 14 mV/m. We note that in the second case, when the electrojet is constrained to flow along the arc, not only E_x but also E_y scales with E_{0_x}. For both models the southward motion of the arc is now faster than the plasma motion. However, as soon as the neutral atmosphere does not corotate, $\mathbf{w_{NW}} \neq \mathbf{0}$, the situation can change, in particular for model YPYHXL where the difference between the arc and plasma motion is small.

[59] We have no conjugated radar measurements, so we cannot say for sure what the velocity of the neutral wind was in our case. However, statistical studies based on EISCAT data, conducted by *Brekke et al.* [1994] and *Nozawa and Brekke* [1995], for quiet and disturbed conditions, respectively, suggest that the two particular cases we explored, $\mathbf{w_{NW}} = -\mathbf{w_{ER}}$ and $\mathbf{w_{NW}} = \mathbf{0}$, encompass to a good extent the range of neutral wind velocities typical for winter evening times. *Brekke et al.* [1994, Figure 5b] show that for quiet winter days the neutral wind around 2100 local time has a tendency to blow westward and southward, at a speed of ~ 100–200 m/s, while during disturbed days there is some shift from southward to northward and some additional westward component (*Nozawa and Brekke* [1995, Figure 6]; note that this study neglects the seasonal dependence).

[60] The change in the electric field associated with the neutral wind leads to a significant change in the ionospheric current. For the case of a corotating atmosphere discussed above, the current is reduced to about one half compared with the values in Figure 13, which is a consequence of the same reduction factor in the electric field. There is, however, no change in the peculiar character of the current configuration: the downward and upward FAC sheets remain decoupled in the ionosphere.

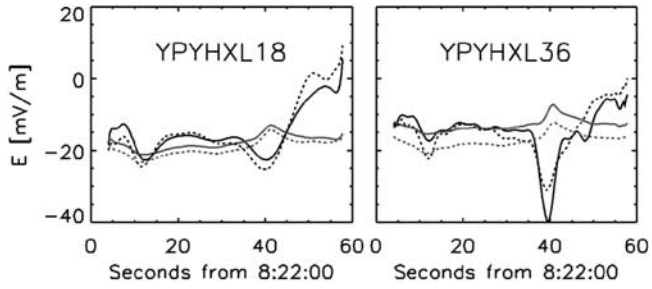

Figure 14. Dependence of the IEF (E_x black, E_y red) on the conductance pattern for model YPYHXL: full distribution (solid) and loss cone (dashes). See color version of this figure at back of this issue.

6.2. Dependence of c_0 on η

[61] In writing equation (19) and further equation (20), we assumed the dependence of c_0 on η can be neglected. This approximation may be questioned when the variation of η along the satellite path, $\Delta\eta = |\sin\theta|L$, is not negligible compared with the length scale, L_η, of the electrojet. It is interesting to see what changes if, instead of taking $c(\eta) = c_0$, we approximate $c(\eta)$ by its Taylor expansion up to the first order

$$c(\eta) = c_0 + \left.\frac{dc}{d\eta}\right|_{\eta=\eta_0} \Delta\eta \simeq c_0 + \frac{c_0}{L_\eta}\Delta\eta = c_0 - \frac{c_0 \sin\theta}{L_\eta}\Delta x. \quad (27)$$

With $\eta_0 = x_0 = 0$, we obtain

$$\begin{aligned} H_\eta - J_\xi &= c_0 - \frac{c_0 \sin\theta}{L_\eta} x + \tilde{c_1}\xi \\ &= c_0 + \left(c_1 - \frac{c_0 \sin\theta}{L_\eta}\right) x = c_0 + \hat{c_1} x, \end{aligned} \quad (28)$$

which, as far as the fit is concerned, does not differ from equation (19). However, the value $\hat{c_1}$ obtained by fit includes a contribution $\delta c_1 \simeq c_0|\sin\theta|/L_\eta$, which can provide an error estimate for c_1 if L_η is evaluated according to equation (18). We found a relative error, $\delta c_1/c_1$, of $\simeq 20\%$ for model YPYHX36 and $\lesssim 8\%$ for model YPYHXL36.

6.3. Dependence of the Results on Conductance

[62] For the models' evaluation we used the conductance obtained by integration over the full velocity space (section 4.1). We have also checked to see what changes when using the conductance obtained by integration over the loss cone. Figure 14 shows the IEF obtained with model YPYHXL and the two conductance estimates. Most of the time the differences are small, implying that the choice of the integration domain is not critical. It is only near $t_0 + 39$, when the conductance drops to very low values, that the

Table 4. Dependence of the Fit Quality on Conductance

	χ_r^2	
Model	Full Distribution	Loss Cone
YPYHXL18	29.1	83.4
YPYHXL36	12.8	29.9

differences become larger for model YPYHXL36, able to resolve this small-scale variation.

[63] It is also interesting to compare the two sets of results from a statistical point of view. The goodness-of-fit parameter, χ_r^2, is listed in Table 4. One can see that the integration over the loss cone leads to higher χ_r^2 values, which imply a lower fit quality. This is not very surprising and supports the use of the full distribution in estimating the conductance.

[64] We have not studied systematically the dependence of the derived IEF on the accuracy of the conductance, but it looks that the error may become important for small-scale inserts of low conductance, even if the calculated conductance there is barely sensitive to the integration domain. On the other hand we did not find substantial differences for the interval I1, where the conductance depends significantly on the integration domain (Figure 5). We note that during I1 there is a strong gradient in the electron precipitation, which leads to errors in the actual conductance because the assumption of stationarity, implicit in equation (24), presumably breaks. Nevertheless, since the derived IEF seems to be not very sensitive to the exact value of the conductance, the impact of these errors on the fit results is probably reduced.

[65] The fit formula, equation (22), also depends on the error, σ_k, assumed for the right-hand side term of equation (20), dependent in its turn on the errors in Σ_P, E_{0_x}, and H_y. In order to evaluate its influence we checked how the fit results change when the weighting factor, $1/\sigma_k$, is dropped. The differences found were minor, except again for the low conductance interval around t_0 + 39, which points to the association of a larger uncertainty in the results with a low conductance.

6.4. Boundary Effects

[66] We have seen in section 5.2 that abrupt variations of the electric field can be sometimes noticed at the boundaries of the fit interval (Figure 10). Closely related to this feature is the dependence of the derived IEF on the fit interval.

[67] Although we do not have a good analytic proof, we feel that the origin of the problem can be traced back to the steep variation of the orthogonal polynomials at the boundaries of the interval, the steeper the higher the order of the polynomial is. Small errors in the polarization coefficients a_i can combine "in phase" with the large variations in G_i, leading to the deviations observed. It would be probably safe to disregard the "boundaries" of the interval, i.e., the two half-periods were the steep variation is concentrated. When the conductance is small and the errors presumably large, it may happen that the boundary errors propagate deeper inside the investigated interval (this is probably the case with the interval I4 in Figure 10).

[68] Function expansion in series of orthogonal polynomials provides, as a rule, only convergence "in the mean" but not uniform convergence [e.g., *Courant and Hilbert*, 1953, p. 54]. The series converges to the approximated function most of the time, but there are also points of poor convergence or no convergence at all.

7. Summary and Prospects

[69] In the present paper we developed a new method, ALADYN, by which it is possible to determine the ionospheric electric field and current in the vicinity of an auroral arc. ALADYN is based on the current continuity equation and on a parametric arc model, incorporates an extended set of satellite data taken well above the current closure region, and can be used over time periods that include traversals of the AAR. The results derived from satellite data can be cross-checked when ground data are available.

[70] We illustrated the method by a detailed examination of a wide, stable, wintertime evening arc. In order to clarify the importance of the parameters, we explored several instances of the arc model, depending on reduced parameter sets. We found that the minimum set of parameters needed for a consistent characterization of the arc includes the polarization, the longitudinal electric field, and the FAC-EJ coupling, even if the arc is reasonably quiet and homogeneous, as the one we used as a test bed. The FAC-EJ coupling coefficient allows the quantitative evaluation of the 2-D ionospheric current flow in the vicinity of the satellite footprint across the arc.

[71] The work can be continued in several directions. ALADYN might be applied to the downward current region and/or summertime conditions, by incorporating the conductance induced by proton precipitation and/or solar radiation. The fit procedure may be updated by using curvilinear instead of cartesian coordinates, as well as by allowing some variation of the longitudinal electric field across the arc. In nonstationary cases, i.e., when the auroral structure has a significant variation during the satellite crossing, a different procedure to estimate the ionospheric potential drop is required.

[72] Event-oriented as well as statistical studies on auroral arcs and eventually also on other auroral forms might be conducted with ALADYN. By future improvements and systematic use ALADYN may become a reliable routine tool for the remote sensing of the high-latitude ionosphere.

[73] **Acknowledgments.** O.M. acknowledges the hospitality of Max-Planck-Institut für extraterrestrische Physik, Garching, which supported this work through several Promotions- and Forschungsstipendiums. The work in Romania was covered by the projects FIRE and PROSPERO, contracts 15/2001 and 72/2003, program Aerospaţial. O.M. is also thankful to Joachim Vogt and Joshua Semeter for fruitful discussions. The mapping of the satellite footprint into the image plane in Figure 4 was done by Joachim. The name ALADYN was coined by Rodica Oanţă-Marghitu. Constructive criticism from the referees is also acknowledged.

[74] Arthur Richmond thanks Tomas Karlsson and Kirsti Kauristie for their assistance in evaluating this paper.

References

Aikio, A., H. Opgenoorth, M. Persson, and K. Kaila (1993), Ground-based measurements of an arc-associated electric field, *J. Atmos. Terr. Phys.*, *55*, 797–808.

Amm, O. (2002), Method of characteristics for calculating ionospheric electrodynamics from multisatellite and ground-based radar data, *J. Geophys. Res.*, *107*(A10), 1270, doi:10.1029/2001JA005077.

Atkinson, G. (1982), Inverted V's and/or discrete arcs: A three-dimensional phenomenon at boundaries between magnetic flux tubes, *J. Geophys. Res.*, *87*, 1528–1534.

Boström, R. (1964), A model of the auroral electrojets, *J. Geophys. Res.*, *69*, 4983–4999.

Brekke, A., S. Nozawa, and T. Sparr (1994), Studies of the E region neutral wind in the quiet auroral ionosphere, *J. Geophys. Res.*, *99*, 8801–8825.
Carlson, C., R. Pfaff, and J. Watzin (1998), The Fast Auroral SnapshoT mission, *Geophys. Res. Lett.*, *25*, 2013–2016.
Coroniti, F., and C. Kennel (1972), Polarization of the auroral electrojet, *J. Geophys. Res.*, *77*, 2835–2851.
Courant, R., and D. Hilbert (1953), *Methods of Mathematical Physics*, Wiley-Interscience, Hoboken, N. J.
de la Beaujardière, O., R. Vondrak, and M. Baron (1977), Radar observations of electric fields and currents associated with auroral arcs, *J. Geophys. Res.*, *82*, 5051–5062.
de la Beaujardière, O., R. Vondrak, R. Heelis, W. Hanson, and R. Hoffman (1981), Auroral arc electrodynamic parameters measured by AE-C and the Chatanika radar, *J. Geophys. Res.*, *86*, 4671–4685.
Ergun, R., L. Anderson, D. Main, Y.-J. Su, C. Carlson, J. McFadden, and F. Mozer (2002), Parallel electric fields in the upward current region of the aurora: Indirect and direct observations, *Phys. Plasmas*, *9*, 3685–3704.
Evans, D., N. Maynard, J. Troim, T. Jacobsen, and A. Egeland (1977), Auroral vector electric field and particle comparisons: 1. Electrodynamics of an arc, *J. Geophys. Res.*, *82*, 2235–2249.
Frey, H., W. Lieb, O. Bauer, H. Höfner, and G. Haerendel (1996), CCD-camera system for stereoscopic optical observations of the aurora, in *Current Developments in Optical Design and Engineering VI*, *SPIE Proc. 2863*, pp. 460–466, SPIE, Bellingham, Wash.
Galand, M., T. Fuller-Rowell, and M. Codrescu (2001), Response of the upper atmosphere to auroral protons, *J. Geophys. Res.*, *106*, 127–139.
Glassmeier, K.-H. (1987), Ground-based observations of field-aligned currents in the auroral zone: Methods and results, *Ann. Geophys.*, *5A*, 115–126.
Haerendel, G., S. Buchert, C. La Hoz, B. Raaf, and E. Rieger (1993), On the proper motion of auroral arcs, *J. Geophys. Res.*, *98*, 6087–6099.
Janhunen, P., A. Olsson, O. Amm, and K. Kauristie (2000), Characteristics of a stable arc based on FAST and MIRACLE observations, *Ann. Geophys.*, *18*, 152–160.
Karlsson, T. (2001), Auroral electric fields from satellite observations and numerical modelling, Ph.D. thesis, Alfvén Lab., Royal Inst. of Technol., Stockholm.
Marghitu, O. (2003), Auroral arc electrodynamics with FAST satellite and optical data, Ph.D. thesis, Tech. Univ. Carolo-Wilhelmina, Braunschweig. (Available at http://www.biblio.tu-bs.de/ediss/data/20030606a/20030606a.html.)
Marklund, G. (1984), Auroral arc classification scheme based on the observed arc-associated electric field pattern, *Planet. Space Sci.*, *32*, 193–211.
McFadden, J., et al. (1998), Spatial structure and gradients of ion beams observed by FAST, *Geophys. Res. Lett.*, *25*, 2021–2024.
Mozer, F. (1971), Origin and effects of electric fields during isolated magnetospheric substorms, *J. Geophys. Res.*, *76*, 7595–7608.
Nozawa, S., and A. Brekke (1995), Studies of the E region neutral wind in the disturbed auroral ionosphere, *J. Geophys. Res.*, *100*, 14,717–14,734.
Opgenoorth, H., I. Häggström, P. Williams, and G. Jones (1990), Regions of strongly enhanced perpendicular electric fields adjacent to auroral arcs, *J. Atmos. Terr. Phys.*, *52*, 449–458.
Pfaff, R., C. Carlson, J. Watzin, D. Everett, and T. Gruner (2001), An overview of the Fast Auroral SnapshoT (FAST) satellite, *Space Sci. Rev.*, *98*, 1–32.
Robinson, R., R. Vondrak, K. Miller, T. Dabbs, and D. Hardy (1987), On calculating ionospheric conductances from the flux and energy of precipitating electrons, *J. Geophys. Res.*, *92*, 2565–2569.
Sesiano, J., and P. Cloutier (1976), Measurements of field-aligned currents in a multiple auroral arc system, *J. Geophys. Res.*, *81*, 116–122.
Sonnerup, B., and M. Scheible (1998), Minimum and maximum variance analysis, in *Analysis Methods for Multi-Spacecraft Data*, *ISSI Sci. Rep.*, vol. 1, edited by G. Paschmann and P. Daly, Int. Space Sci. Inst./Eur. Space Agency, Bern, Switzerland.
Sugiura, M. (1984), A fundamental magnetosphere-ionosphere coupling mode involving field-aligned currents as deduced from DE-2 observations, *Geophys. Res. Lett.*, *11*, 877–880.
Untiedt, J., and W. Baumjohann (1993), Studies of polar current systems using the IMS Scandinavian magnetometer array, *Space Sci. Rev.*, *63*, 245–390.

G. Haerendel, International University of Bremen, Campus Ring 1, D-28725 Bremen, Germany. (hae@iu-bremen.de)
B. Klecker, Max-Planck-Institut für extraterrestrische Physik, D-85748 Garching, Germany. (berndt.klecker@mpe.mpg.de)
O. Marghitu, Institute for Space Sciences, P.O. Box MG-23, RO-77125 Bucharest, Romania. (marghitu@venus.nipne.ro)
J. McFadden, Space Sciences Laboratory, University of California, Berkeley, CA 94720, USA. (mcfadden@ssl.berkeley.edu)

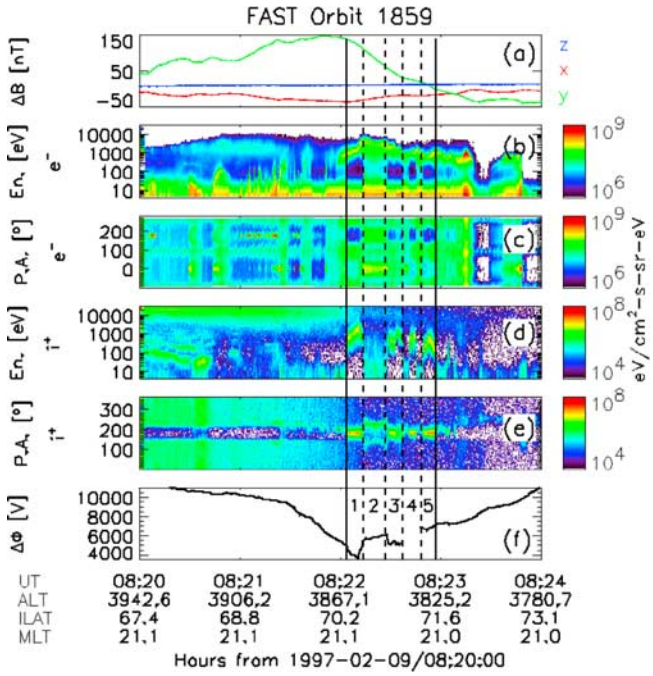

Figure 3. Medium-scale DC electromagnetic field and particles; the solid vertical lines indicate the ion beam interval, IALL, that will be used for the illustration of ALADYN; the dashed vertical lines show the subintervals I1–I5 (cf. Table 3). From top to bottom the figure shows (a) perturbation magnetic field, (b–e) electron/ion energy and pitch-angle spectrograms, and (f) potential drop along the satellite track. In Figures 3c and 3e the pitch-angle covers 360°, corresponding to the plasma instrument field of view; the angle range is shifted by 90° in Figure 3c to avoid having downward electrons split up among the plot borders. For the data gap in Figure 3f, see text.

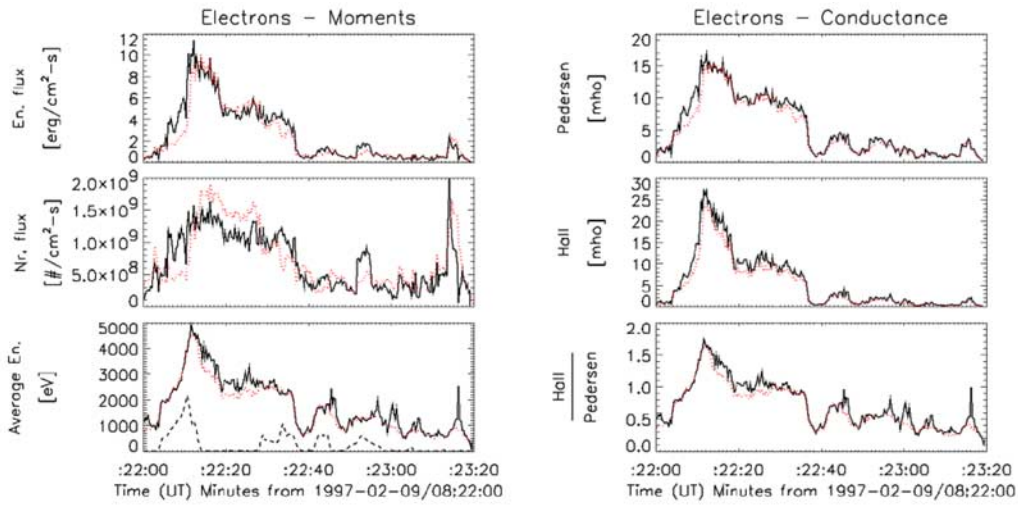

Figure 5. (left) Electron energy flux, number flux, and average energy, at ionospheric level, under the inverted-V. (right) Σ_P, Σ_H, and the ratio Σ_P/Σ_H, calculated from equation (24), by using Φ_W and $\overline{W}$ from the left plot. Black solid lines (red dots) indicate integration over the full velocity space (loss cone). In the bottom left panel the ion beam average energy is shown with black dashes.

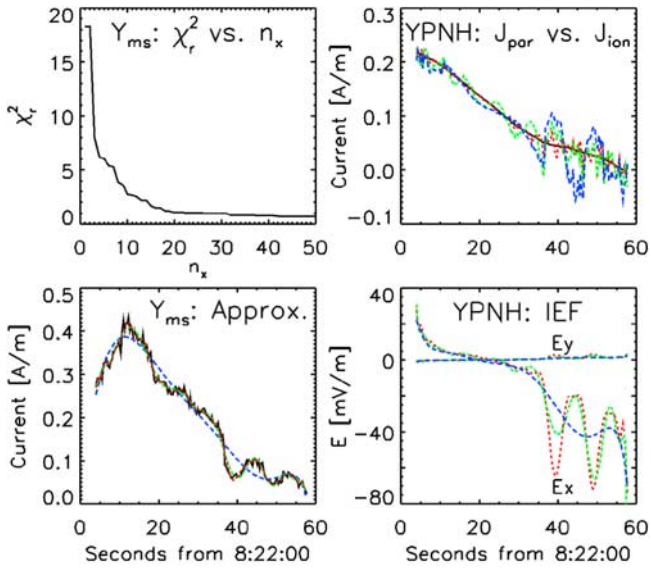

Figure 7. (top left) Dependence of χ_r^2 on the expansion order for y_{ms}. (bottom left) Approximations of the measured data, y_{ms} (black solid), with orthogonal polynomials. (right) Fit results obtained for model YPNH; J_{par} is plotted black solid. In the bottom left and in the right panels blue long-dashes/green dash-dots/red dashes stand for n_x = 7/18/36.

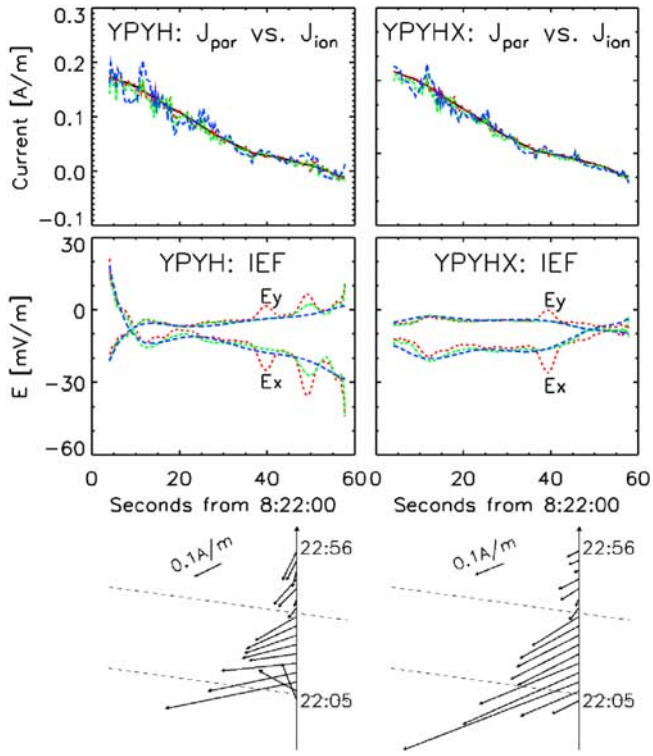

Figure 8. Fit results obtained for models YPYH (left) and YPYHX (right). (top) Fit quality, J_{par} versus J_{ion}; (middle) Electric field for n_x = 7/18/36; (bottom) Ionospheric current along the satellite footprint for n_x = 36. The color-line style convention in the top and middle panels is the same as in Figure 7.

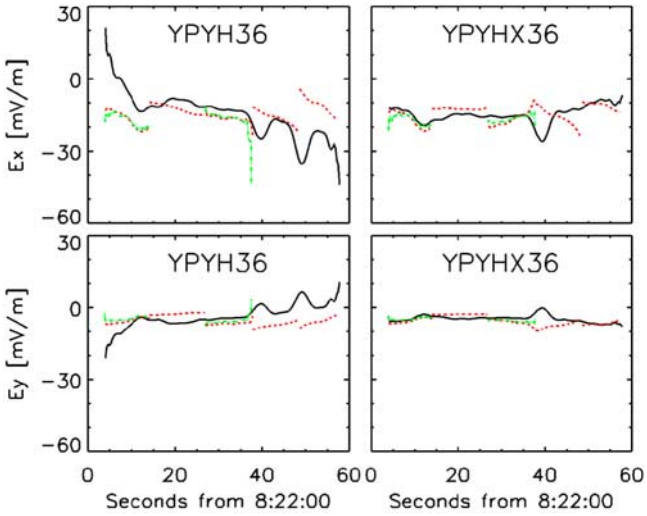

Figure 10. Internal consistency check for the models YPYH (left) and YPYHX (right): E_x (top) and E_y (bottom) obtained from fit over IALL (black solid) and over the subintervals I1–I5 (red dashes). The fit over I1 and I3 was also performed with Burst data, available during these intervals (green dash-dots).

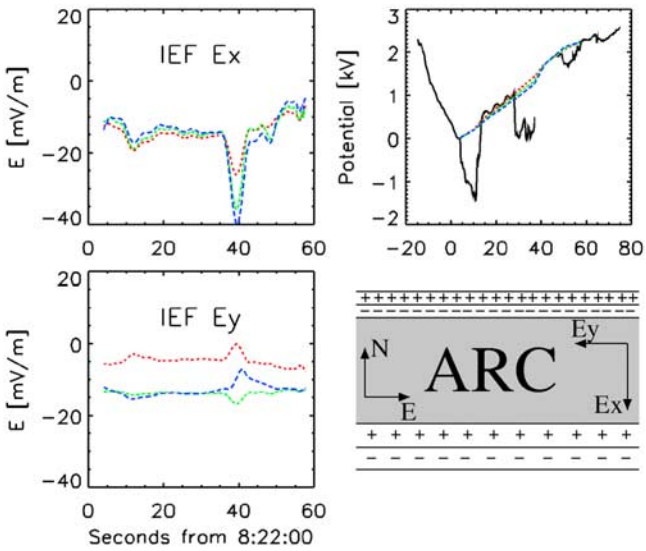

Figure 11. Comparison between the ionospheric electric field and potential obtained with models YPYHX36 (red dashes) and YPYHXL36, by applying minimum variance analysis over IALL (green dash-dots) and over a sliding 10 s window (blue long dashes). In the top right panel the high-altitude potential (black solid) is plotted for reference. The bottom right panel shows an outline of the arc, including the polarization charge double layers associated with the divergence of the electric field at the arc edges. At the southern edge of the arc the double layer is wider and less intense than at the northern edge, as indicated by the E_x panel.

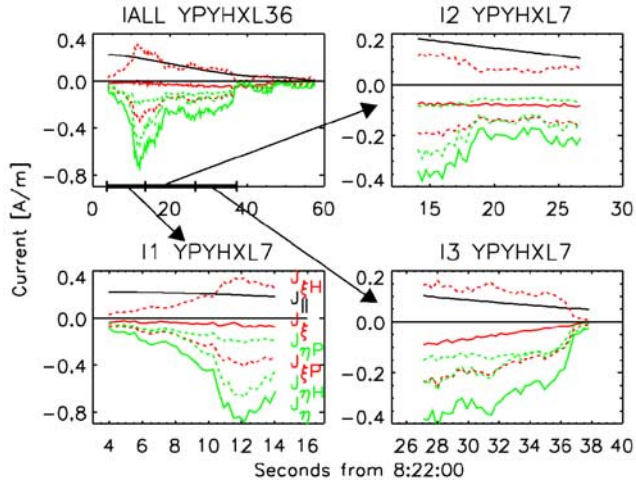

Figure 13. The FA and ionospheric sheet currents, along the FAST footprint, resulting from model YPYHXL. The Pedersen and Hall components of J_ξ (red) and J_η (green) are shown with dashed lines and are labeled in the bottom left panel. (top left) Fit over IALL. (bottom and top right) Fit over the intervals I1, I2, and I3 that encompass the visible arc. J_ξ during I1 is very small, indicating a negligible ionospheric current transfer between the downward and upward FACs.

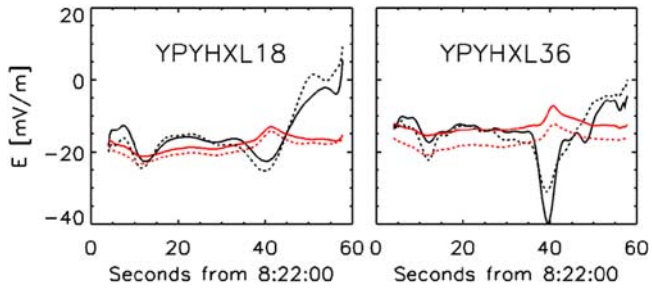

Figure 14. Dependence of the IEF (E_x black, E_y red) on the conductance pattern for model YPYHXL: full distribution (solid) and loss cone (dashes).